

## Instruments and Methods

# Improved method to determine radio-echo sounding reflector depths from ice-core profiles of permittivity and conductivity

Olaf EISEN,<sup>1,2</sup> Frank WILHELMS,<sup>1</sup> Daniel STEINHAGE,<sup>1</sup> Jakob SCHWANDER<sup>3</sup>

<sup>1</sup>*Alfred-Wegener-Institut für Polar- und Meeresforschung, Postfach 120161, D-27515 Bremerhaven, Germany  
E-mail: oeisen@awi-bremerhaven.de*

<sup>2</sup>*Versuchsanstalt für Wasserbau, Hydrologie und Glaziologie, Eidgenössische Technische Hochschule, ETH-Zentrum, CH-8092 Zürich, Switzerland*

<sup>3</sup>*Physikalisches Institut, Universität Bern, Sidlerstrasse 5, CH-3012 Bern, Switzerland*

**ABSTRACT.** We present a technique that modifies and extends down-hole target methods to provide absolute measures of uncertainty in radar-reflector depth of origin. We use ice-core profiles to model wave propagation and reflection, and then cross-correlate the model results with radio-echo sounding (RES) data to identify the depth of reflector events. Stacked traces recorded with RES near the EPICA drill site in Dronning Maud Land, Antarctica, provide reference radargrams, and dielectric properties along the deep ice core form the input data to a forward model of wave propagation that produces synthetic radargrams. Cross-correlations between synthetic and RES radargrams identify differences in propagation wave speed. They are attributed to uncertainties in pure-ice permittivity and are used for calibration. Removing conductivity peaks results in the disappearance of related synthetic reflections and enables the unambiguous relation of electric signatures to RES features. We find that (i) density measurements with  $\gamma$ -attenuation or dielectric profiling are too noisy below the firn-ice transition to allow clear identification of reflections, (ii) single conductivity peaks less than 0.5 m wide cause the majority of prominent reflections beyond a travel time of about 10  $\mu$ s ( $\sim$ 900 m depth) and (iii) some closely spaced conductivity peaks within a range of 1–2 m cannot be resolved within the RES or synthetic data. Our results provide a depth accuracy to allow synchronization of age–depth profiles of ice cores by RES, modeling of isochronous internal structures, and determination of wave speed and of pure-ice properties. The technique successfully operates with dielectric profiling and electrical conductivity measurements, suggesting that it can be applied at other ice cores and drill sites.

## 1. INTRODUCTION

The interpretation of glacial radio-echo sounding (RES) profiles exploits the distribution of reflected energy with travel time, distinct reflection patterns and the absorption and scattering of the radio waves. Profile features are interpreted to locate the ice–bedrock interface, internal layers and other physical transitions like temperature or crystal structure (see, e.g., Siegert, 1999; Lythe and others, 2001; Dowdeswell and Evans, 2004; Matsuoka and others, 2004a). Over recent decades, the coverage of the Greenland and Antarctic ice sheets with RES has considerably increased and it is being further extended within programs like EPICA (European Project for Ice Coring in Antarctica), ITASE (International Trans-Antarctic Scientific Expedition) and the IPY (International Polar Year) scheduled for 2007/08. The depths of internal reflections are often linked to age–depth profiles established along firn and ice cores or within snow pits to investigate recent patterns of accumulation (Richardson and others, 1997; Nereson and others, 2000; Richardson-Näslund, 2001; Frezzotti and others, 2002; Pälli and others, 2002; Eisen and others, 2004; Spikes and others, 2004; Vaughan and others, 2004; Karlöf and others, 2005; Steinhage and others, 2005) or to short- and long-term glaciological processes (Morse and others, 1998; Fahnestock and others, 2001; Leonard and others, 2004; Siegert and others, 2004). Most importantly for paleoclimate research,

several ice-core deep-drilling sites have been (or will be in the near future) stratigraphically linked by RES (e.g. the Antarctic sites Vostok and Dome Concordia (Siegert and others, 1998), EPICA Dronning Maud Land (EDML) and Dome Fuji (Steinhage, unpublished information), and the major Greenland sites GRIP, GISP and NorthGRIP (Dahl-Jensen and others, 1997)). The isochronous properties of most continuous internal reflection horizons detected with RES have the potential to physically link the ice-core profiles, thus providing additional constraints for climatic interpretations. In the context of present research dealing with the evolution of ice sheets and the prediction of their future behavior, spatial age–depth distributions calculated from ice-sheet models (e.g. Clarke and others, 2005) require field data for calibration and validation, which can only be provided by RES profiles.

Although the principal physics and mechanisms underlying RES have been known for a long time (Evans, 1965; Robin and others, 1969; Millar, 1981), improved radar devices and techniques to determine the in situ physical properties have led to progress in understanding the detailed processes that cause reflections. High-resolution data have made it possible to augment the interpretation of ice cores (Jacobel and Hodge, 1995; Dahl-Jensen and others, 1997) and to cross-correlate ice-core profiles and radargrams (Hempel and others, 2000). Improved ice-core profiling has made it feasible to calculate synthetic radargrams by

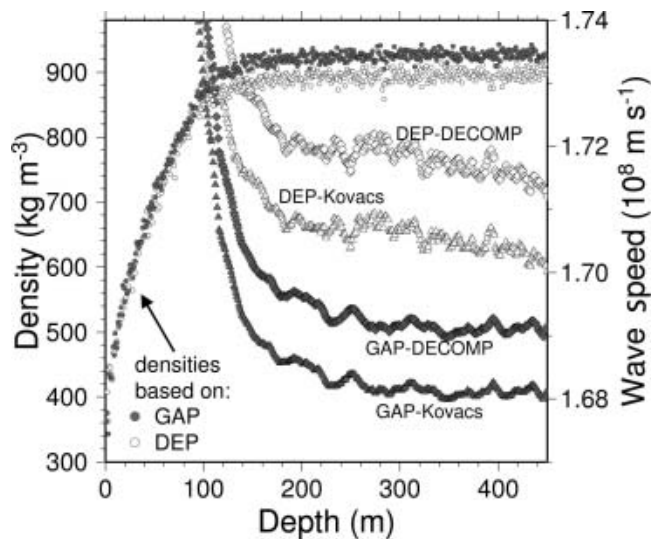


**Fig. 1.** Distribution of density (circles) and wave speed with depth based on  $\gamma$ -attenuation profiling (GAP; filled symbols) and inverted dielectric profiling (DEP; empty symbols) data in top 450 m of ice core. Densities and wave speeds are filtered over 1 and 10 m bins, respectively, with values displayed in 1 m increments. Conversions of density to wave speed are based on the Kovacs and others (1995) approximation (triangles) and DECOMP (Equation (2)) (diamonds).

forward modeling, focusing on the upper parts of the ice column (Moore, 1988; Miners and others, 1997; Kanagaratnam and others, 2001; Eisen and others, 2003; Kohler and others, 2003), but also employing data over the full length of a deep ice core (Miners and others, 2002).

As all RES systems basically yield the data in the domain of travel time, the conversion of travel time to depth is the essential processing step for all quantitative applications. Naturally, the determination of RES reflector depths involves uncertainties. Uncertainties in age estimates along RES profiles are relatively small in the firn column. However, they increase in the deeper parts, where annual layer thickness decreases. The deeper regions are of special interest, because they harbor the oldest ice and contain the largest expressions of ice dynamics. The improvement of depth estimates of RES reflectors is the topic of this paper.

In general, time–depth conversions are based on measured or assumed distributions of wave speed with depth. The most simple way, widely applied, is to use a constant electromagnetic wave speed for solid ice (e.g. Morse, 1997; Siegert and others, 1998; Fahnestock and others, 2001; Matsuoka and others, 2004a; Vaughan and others, 2004). In some cases a correction for the higher wave speed in the firn column is added, varying with geographic location (Dowdeswell and Evans, 2004). Most direct measurements of wave speeds are derived from ice-core profiles of density or permittivity (Robin and others, 1969; Clough and Bentley, 1970; Kovacs and others, 1995; Richardson and others, 1997; Eisen and others, 2002) or tomography between boreholes or pits (Fortin and Fortier, 2001; Kravchenko and others, 2004). Indirect measurements depend on knowledge of reflector depth and travel time, as is needed for down-hole radar methods (Jezek and Roeloffs, 1983; Clarke and Bentley, 1994), or on a defined survey geometry for wide-angle reflection measurements (Annan and Davis, 1976) and common-midpoint surveys

(Fisher and others, 1992; Hempel and others, 2000; Murray and others, 2000; Eisen and others, 2002).

Wave speeds in snow, firn and ice mainly depend on density (Bogorodsky and others, 1985). A recent compilation of the few available wave-speed measurements in ice for the Antarctic continent (Popov and others, 2003), however, demonstrates that a spatial variation on the order of 3% seems to exist. Furthermore, there are various models available that relate density and permittivity, which are used for the conversion of density measured along an ice core to wave speed. The determination of wave speed from ice-core measurements depends sensitively on the choice made and the device used for density measurements because results differ on the order of 1% (Fig. 1). Any uncertainties in wave speed from density or permittivity translate to a relative uncertainty in depth, which implies an increasing absolute error with travel time and depth. For deep reflections depth errors can therefore be large enough to significantly influence the geophysical interpretation. Among the methods mentioned above, the down-hole radar technique is the only means that directly establishes a time–depth relationship without using information of wave-speed distribution. Therefore, it has to be considered the most accurate method. All other approaches indirectly relate time to depth by integrating a wave-speed distribution, and are thus subject to cumulating errors with depth.

The objective of this paper is to develop a new accurate method to determine the depth of RES reflections. We feed ice-core data to a numerical model of electromagnetic wave propagation to generate synthetic radargrams, and then cross-correlate the radargrams with RES profiles to determine depths. In this way we avoid the propagation of errors in wave speed that may be introduced by first determining the wave-speed distribution and then integrating it to relate travel time and depths. We test our method with data from EPICA in Dronning Maud Land (75° S, 0° E), where 2565 m of a deep ice core (EDML) had been retrieved by 2004, with about 210 m left to bedrock. Physical properties are available from dielectric profiling (DEP) (Moore and Paren, 1987) to provide permittivity and conductivity for RES interpretation. From sensitivity studies we identify the origin of depths of unambiguous, distinct reflection characteristics present in the RES and synthetic radargrams. These are then linked to the observed travel time of the reflection. Thus, in principle, our approach is comparable to down-hole target techniques.

We find that single conductivity peaks are mostly responsible for individual reflections, especially in the intermediate and deeper parts of the ice sheet. This is contrary to earlier findings, that only closely spaced boundaries of dielectric interfaces lead to internal reflections at greater depth in ice sheets (Millar, 1982; Siegert and others, 1998) and similar implications for ice streams (Jacobel and others, 1993). By-products are in situ permittivity of pure ice and mean wave speed.

We first introduce the ice-core measurements, followed by a description of the RES data and the modeling approach, including a detailed layout of several processing steps for the input data. The main part of the paper treats the identification of reflector depths by sensitivity studies and discusses the results. Utilization of permittivity and conductivity profiles measured with different devices leads us to the conclusion that the method can also be applied at other sites.

## 2. ICE-CORE MEASUREMENTS

In the field  $\gamma$ -attenuation profiling (GAP) and DEP were used to simultaneously measure density and dielectric properties along the EDML ice core. The system and bench fixture, performance and measurement uncertainties are described by Wilhelms (2000). Electrical conductivity measurements (ECM) (Hammer, 1980) were performed along the EDML ice core during ice-core processing and cutting in the cold room after the core was transported to the Alfred Wegener Institute in Bremerhaven, Germany.

### 2.1. GAP ( $\gamma$ -attenuation profiling)

The absorption and scattering of  $\gamma$ -rays originating from a radioactive source ( $^{137}\text{Cs}$ ) and passing in the transverse direction through the ice core to the detector (Wilhelms, 1996, 2000) are used for  $\gamma$ -attenuation profiling. The radiation is monochromatic and thus the mass absorption coefficient is known with 0.1% relative error. The statistical intensity measurement errors of the free-air reference and at each sampling position are determined from direct analysis of the recorded data collection of at least 20 measurements. The calibrated detector signal is corrected for variations in core diameter. Furthermore, the possible influence at maximum misalignment of the core within the bench is estimated and a propagation of error is performed for each single measurement. The precision of the density measurement is typically in the range 0.006–0.01  $\text{g cm}^{-3}$  for a 100 mm diameter core. Unreliable data in the vicinity of core breaks are removed from the dataset. Along the EDML ice-core density was measured to 450 m depth in 5 mm increments (Fig. 1).

### 2.2. DEP (dielectric profiling)

We express the complex parts of the relative dielectric permittivity as

$$\varepsilon^* = \varepsilon' - i\varepsilon'' \quad (1)$$

where the real part,  $\varepsilon'$ , is the ordinary relative permittivity of the medium. The imaginary part, the dielectric loss factor, is related to conductivity,  $\sigma$ , and radian frequency,  $\omega$ , by  $\varepsilon'' = \sigma(\varepsilon_0\omega)^{-1}$ , where  $\varepsilon_0$  is the permittivity of free space. Both parts of  $\varepsilon^*$  can be determined with DEP (Moore and Paren, 1987). An improved DEP scanner (Wilhelms, 2000), operating at 250 kHz, was used over the full depth of the EDML ice core (2565.55 m). The upper 12.6 m of the dataset are missing because of the operational set-up of the deep drilling. They are replaced by adjusted profiles of the shallow ice core B32, located 1.5 km to the west. The calibrated DEP record is corrected for variations in core diameter and temperature. Unreliable data in the vicinity of core breaks, as for GAP, are removed. The correct interpretation of DEP requires that the effects of mixing of air and ice are taken into account. This is done by applying the formula for density and conductivity mixed permittivity (Wilhelms, 2005) explained below.

### 2.3. ECM (electrical conductivity measurements)

ECM is essentially a measure of d.c. conductance. It has traditionally been carried out by dragging a pair of electrodes with a high voltage between them along a core, and measuring the current between the electrodes (Hammer, 1980; Neftel and others, 1985). A new ECM system, developed at the University of Bern, was used in the field

at Dome Concordia (Wolff and others, 1999) and later in the laboratory for measuring the EDML ice core. In brief, a flat surface is prepared in the ice-core processing line along its full length using a horizontal band-saw and a microtome knife. The electrode assembly consists of seven electrodes at an inter-electrode spacing of 8 mm across the core. The electrodes are made of a carbon-doped silicon rubber. They are lowered onto the flat surface of the core and 350 V is applied across each adjacent pair of electrodes in turn. The current between the electrodes is sampled at regular intervals after a settling time, and averaged. The electrodes are lifted and moved 1 mm along the core and the sequence is repeated. This procedure yields six sets of data at 1 mm resolution. The data presented here are averaged over 10 mm and corrected to  $-15^\circ\text{C}$ . Documented major core breaks and ends are removed from the ECM record. To date, corrected ECM data are available along the EDML ice core from 113.01 to 2563.98 m depth.

### 2.4. DECOMP (density and conductivity mixed permittivity)

Kovacs and others (1995) match a comprehensive dataset with a simple empirical formula relating the ordinary relative permittivity  $\varepsilon'$  to density  $\rho$ :  $\varepsilon' = (1 + 0.845\rho)^2$ . They obtain a standard error of  $\pm 0.031$  for  $\varepsilon'$ , about 1% of the permittivity of pure ice (i.e. ice without bubbles and impurities). Looyenga (1965) derives a theoretical mixing model for air distributed in a dielectric medium based on spherical approximations of bubbles. Extension of his relation to complex space (Wilhelms, 2005) leads to

$$\varepsilon^{*1/3} = \frac{\rho}{\rho_{\text{ice}}} \left[ \left( \varepsilon'_{\text{ice}} - i \frac{\sigma_{\text{ice}}}{\omega \varepsilon_0} \right)^{1/3} - 1 \right] + 1, \quad (2)$$

where the subscript 'ice' refers to values of the pure-ice (i.e. bubble-free) volume fraction, taking into account impurities that contribute to conductivity, like acids. Variables without a subscript refer to bulk values of the ice–air mixture. Wilhelms (2005) demonstrates that neglect of complex mixing for the density–permittivity relation could result in significant errors in  $\varepsilon^*$ . Combination of  $\gamma$ -attenuation density and DEP data for the upper 450 m of the EDML core, analogously to Wilhelms (2005), yields  $\varepsilon'_{\text{ice}} = 3.094$  and  $\rho_{\text{ice}} = 926 \text{ kg m}^{-3}$ . Based on these values for the pure-ice fraction, which are the most consistent available for our site, we numerically invert Equation (2) to derive density and conductivity from the DEP measurements at 250 kHz (Fig. 1). Directly applying Equation (2) to the inverted DEP density and conductivity yields  $\varepsilon^*$  at 150 MHz, assuming that  $\varepsilon'$  does not change with frequency. This is done for the combinations of density (GAP and DEP) and DEP conductivity shown in Table 1. Each combination serves as input to a run of the wave-propagation model described below and results in a synthetic trace, designated  $S_i$  ( $i = 1, \dots, 5$ ) (Table 1). For ice, a Debye relaxation occurs below 10 kHz (Bittelli and others, 2004). Its tail causes a tiny frequency dependence of complex permittivity  $\varepsilon^*$  in the MHz range (Fujita and others, 2000, figs 2 and 3). Our calibration of the pure-ice permittivity described later implicitly takes care of this small effect for  $\varepsilon'$ . Moreover, Equation (2) suffices to scale the conductivity with frequency, as the Debye relaxation frequency has been found to be constant near and at conductivity peaks (Wilhelms, unpublished data).

**Table 1.** Description of radargram origin

	Density	Conductivity	$\epsilon'_{ice}$	$l(\epsilon')$ m	$\sigma$ peaks
Synthetic radargram					
$S_1$	DEP	DEP	3.09	0.2	–
$S_2$	GAP	DEP	3.09	0.2	–
$S_3$	DEP	DEP	3.09	20	–
$S'_3$	DEP	DEP	3.20	20	–
$\tilde{S}'_3$	DEP	DEP	3.20	20	li
$S_4$	GAP	DEP	3.09	20	–
$S_5$	DEP	ECM	3.09	20	–
$S'_5$	DEP	ECM	3.20	20	–
$\tilde{S}'_5$	DEP	ECM	3.20	20	li
Reference radargram					
$R_1$	trace 4204 of airborne RES profile 023150				
$R_2$	stack of ground-based RES profile 033042				

Notes: Plain symbols,  $S_n$ , imply  $\epsilon' = 3.09$ ; primed symbols,  $S'_n$ , imply  $\epsilon' = 3.20$ ; symbols with a tilde,  $\tilde{S}'_n$ , and li indicate that selected conductivity peaks in  $\epsilon'$  are removed and the gaps are linearly interpolated for the sensitivity studies;  $l(\epsilon')$  indicates the filter length for  $\epsilon'$ . Details are given in the text.

ECM measurements along the EDML core were not carried out simultaneously with GAP and DEP, therefore restricting the use of Equation (2). An exact transfer of measured d.c.-ECM conductivity values to the frequency of radio waves requires knowledge of chemical composition and frequency-dependent properties of the constituents (Moore and others, 1992, 1994). Moreover, ECM is not a direct measure of electrical d.c. conductivity, as currents depend on the contact area of the electrodes which is difficult to keep constant, and are predominantly influenced by the conductivity in the vicinity of the contact area. ECM currents are also affected by electrode polarization (Maidique and others, 1971). For our 'proof-of-concept' study, which is based on conductivity changes rather than on the absolute values, we choose a simpler approach. We scale the ECM record so that the mean ECM conductivity equals the mean DEP conductivity, the latter corrected for dielectric mixing and transferred to the MHz range, so that their means agree over the whole depth range. For all model runs  $S_5$  (Table 1) the DEP-conductivity data are then replaced by the scaled ECM-conductivity record.

### 3. LINKING RES DATA TO ICE-CORE PROFILES

Based on combinations of the above ice-core records we calculate synthetic radargrams. After calibrating in situ properties of the pure-ice fraction within their uncertainty range by comparing the synthetic radargrams to measured RES reference data, we perform sensitivity studies to identify the origin of individual reflections.

#### 3.1. Reference radargrams from airborne RES

We use RES data obtained with the Alfred Wegener Institute airborne system operated on the *Polar2*, a Dornier 228-101 aircraft, from Antarctic seasons 2002 and 2003. The system generates a 150 MHz burst of 60 ns duration with a peak power of 1.6 kW and 20 MHz bandwidth (Nixdorf and

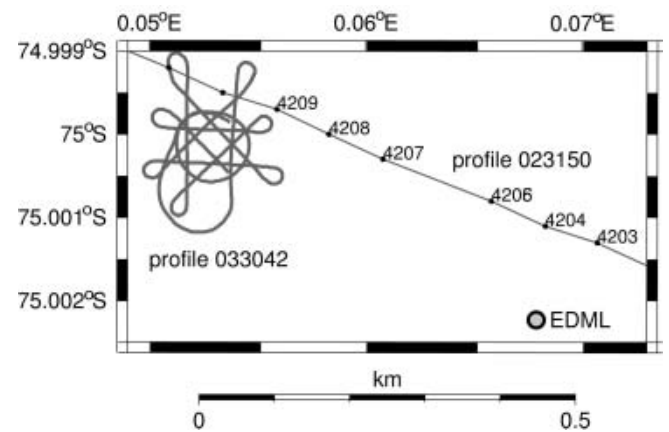


**Fig. 2.** Location of airborne profile 023150 and of ground-recorded profile 033042. The numbers refer to 10-fold stacked traces along profile 023150. The circle indicates the position of the EPICA drilling site. Reference radargram  $R_1$  corresponds to trace number 4204, which is closest to the drilling site.  $R_2$  is calculated from stacking all  $\sim 14\,000$  traces of profile 033042.

others, 1999). The receiver system includes a logarithmic amplifier and rectifies the received signal, i.e. the phase information is not recovered. An analog-to-digital converter samples at an interval of 13.33 ns and records over a window of 50  $\mu$ s. Two hundred consecutive traces are stacked and the averaged traces are stored on tape. The overall system performance figure is 190 dB. During airborne surveys the ground speed is 65  $\text{m s}^{-1}$  (130 knots), resulting in a trace spacing of 6.5 m (Nixdorf and others, 1999).

Two RES profiles are considered, the locations of which are displayed in Figure 2. Profile 023150 was recorded during flight at an altitude of 450 m. It runs parallel to the ice divide in an east-southeast–west-northwest direction and passes the drilling location at a distance of  $\sim 100$  m to the north-northeast. Horizontal stacking was applied to ensembles of ten consecutive traces stored on tape. The stacked trace 4204 is used as reference radargram  $R_1$ . To provide a higher spatial coverage and at the same time avoid uncertainties in the orientations of the airplane during flight, profile 033042 was recorded with the airplane sliding on the ground. An area of  $200 \times 300 \text{ m}^2$  about 500 m west-northwest of the drilling site was covered with some 14 000 traces recorded with multiple orientations of the airplane. Stacking of all traces results in the reference radargram  $R_2$ . No additional filtering or gain control is applied to the RES data. The reference radargrams  $R_{1,2}$  (Fig. 3) are shifted in time such that their first break (the reflection from the surface) occurs at 0. We omit the time interval 0–2  $\mu$ s as the strength of the surface reflection saturated the RES system receiver.

It is obvious from Figure 3 that the signal-to-noise ratio (SNR) in  $R_2$  is remarkably lower than in  $R_1$  because of the much higher stacking coverage. Despite the higher SNR, maximum amplitudes of reflections are slightly lower than for  $R_1$  for two reasons. First, the profile 033042 covers an area that is larger than the first Fresnel zone of the transmitted wave. Second, the stacked traces were recorded with different antenna orientations, and thus did not take account of the anisotropic and birefringent properties of the ice (Hargreaves, 1978; Fujita and others, 2000). Both these contribute to destructive interference and thus lower

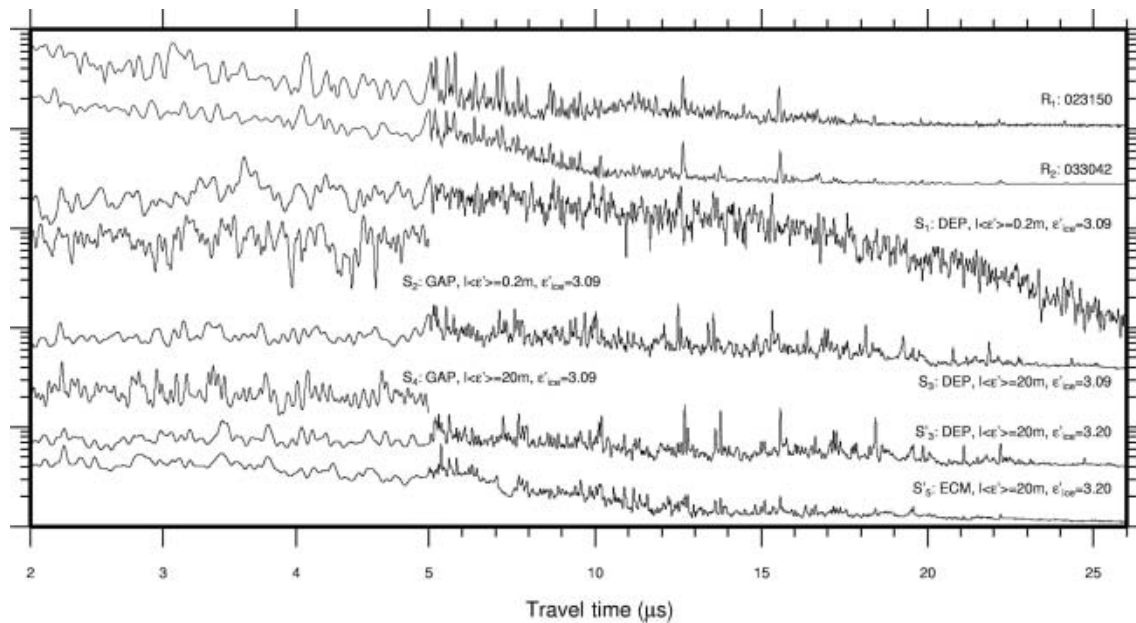


**Fig. 3.** Comparison of RES- and FD-radargram envelopes on a logarithmic scale (arbitrary units). From top to bottom: trace 4204 of profile 023150 ( $R_1$ ); 14 000-trace stack of profile 033042 ( $R_2$ ); nomenclature of synthetic radargrams (Table 1): plain symbols,  $S_i$ ;  $\epsilon' = 3.09$ ; primed symbols,  $S'_i$ ;  $\epsilon' = 3.20$ ;  $l(\epsilon')$  indicates the filter length for  $\epsilon'$ ; specifically:  $S_1$  and  $S_2$  are based on DEP and GAP profiles, respectively, and using  $\epsilon'_{ice} = 3.094$  and a 0.2 m running mean filter applied to  $\epsilon'$  (indicated by  $l(\epsilon')$ );  $S_3$  and  $S_4$ , which are the same as  $S_1$  and  $S_2$ , respectively, but with a 20 m running mean filter applied to  $\epsilon'$ ;  $S'_3$  and  $S'_4$ , which are the same as  $S_3$  and  $S_4$ , but using  $\epsilon'_{ice} = 3.20$ ; and  $S'_5$  based on DEP-density and ECM-conductivity profiles with  $\epsilon'_{ice} = 3.20$  and  $l(\epsilon') = 20$  m. The magnitude of the synthetic radargrams is linearly scaled with travel time to compensate for the logarithmic pre-amplification of the RES system. Note the different scale of the 2–5  $\mu$ s (the length of the GAP record) and 5–20  $\mu$ s range.

amplitudes. At times  $>18 \mu$ s the reflections are very close to the system noise level, and result in a lower boundary in amplitude with no further decrease with travel time. In this interval, several reflections can be more clearly identified in  $R_2$  than in  $R_1$ . Within each radargram a reflection maximum can be located with an uncertainty of one sample interval ( $\pm 13$  ns). The position of numerous major reflections, rising more than three times above the surrounding magnitude and present in each reference radargram, are in very good agreement with each other. The remaining differences in travel times of temporally corresponding reflections in  $R_1$  and  $R_2$  are most likely caused by the 0.5 km separation of the locations. For the differences in travel time we obtain  $0 \geq \Delta t_{R_2-R_1} \geq -50$  ns for travel times less than 10  $\mu$ s, that is reflections of  $R_1$  occur slightly later than those of  $R_2$ . For travel times beyond 20  $\mu$ s,  $0 \leq \Delta t_{R_2-R_1} \leq 80$  ns, reflections of  $R_1$  occur earlier than those of  $R_2$ .

### 3.2. Calculation of synthetic radargrams

We use a one-dimensional version of the parallelized finite-difference (FD) time-domain model successfully applied to the simulation of shallow ground-penetrating radar radargrams by Eisen and others (2003), which are based on the staggered-grid formulation of Maxwell's curl equations (Yee, 1966). The model operates with a spatial increment of 0.02 m and a time-step of 0.02 ns, ensuring numerical stability and dispersion criteria (Eisen and others, 2003). The data domain extends from 0 to 2565 m (the ice-core length). The model domain is chosen large enough that reflections from the model boundaries do not interfere with physical reflections caused by ice-core properties. Profiles of  $\epsilon^*$  at 150 MHz serve as model input, which are calculated from different combinations of DEP-, GAP- and ECM-based

permittivity and conductivity data introduced above (Table 1).

The rectification and logarithmic amplification of the RES receiver signal prevents the phase retrieval of the signal transmitted into the ice. Theoretically, the 60 ns burst should contain nine sinusoidal waves of 150 MHz. Hardware-related finite rise and decay times of the burst-trigger switches, common for RES transmitters (Matsuoka and others, 2004b), and the limited bandwidth of the transmitter antenna (Nixdorf and others, 1999) lead to signal broadening and changes in the frequency spectrum. This is evident from the envelope shape of the received reflection from the air-ice interface. It has a total width of roughly 140 ns at half maximum, i.e. more than twice the theoretical pulse length (which partly results from reverberations of the surface).

Radargrams produced by wave-propagation modeling as well as real measurements are sensitive to the transmitted signal (e.g. Miners, 1998). Especially long wavelets easily lead to interference and reduced resolution; in the worst case even destructive interference. Unfortunately, the exact characteristics of the radiated wavelet of the airborne system are unknown. We have two aims: first, our main concern is to identify the depth of origin of a reflector at high resolution; and, second, we aim to determine the type of physical signal that causes the reflection. For the first aim a short synthetic source pulse should be used, as a long one could cause a degradation in the quality of the synthetic radargrams, which do not occur in the real measurements. However, our second aim requires a longer pulse, as a short one (e.g. a Ricker wavelet) could not reproduce the physical smoothing effect, i.e. interference, of a longer pulse. As a trade-off we use a synthetic wavelet consisting of only 2.5 150 MHz cycles of unit amplitude for modeling. In addition,

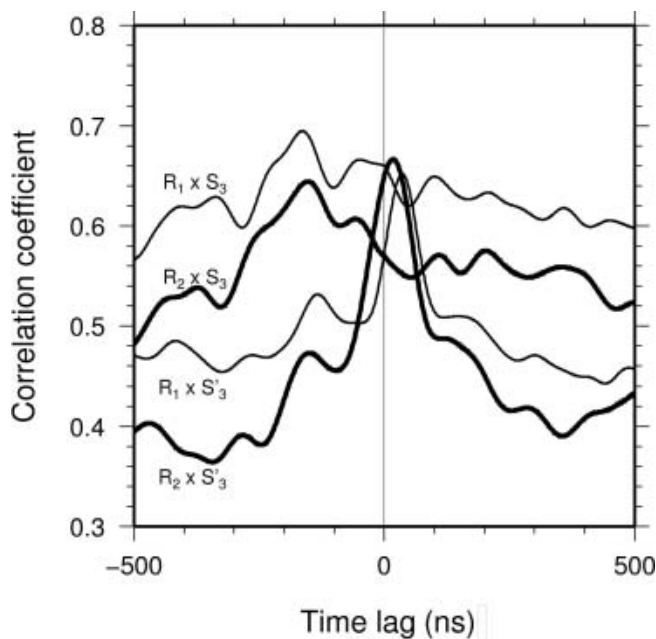


**Fig. 4.** Cross-correlation functions of  $S_3$  ( $\epsilon'_{\text{ice}} = 3.094$ ) and  $S'_3$  ( $\epsilon'_{\text{ice}} = 3.20$ ) with  $R_1$  (thin line) and  $R_2$  (thick line) for the time interval 10–26  $\mu\text{s}$  with a maximum lag of  $\pm 500$  ns.

half-wavelength oscillations of lower amplitude are added that precede and follow the synthetic wavelet, as is typical for burst and pulse radar systems (Miners and others, 2002).

The following processing steps could be regarded as a filtering procedure that aims to conciliate our apparently incompatible aims. To synchronize the occurrence of maximum power of the RES direct coupling signal and the synthetic transmitter signal, the FD radargrams are shifted by +0.1  $\mu\text{s}$ . Further processing includes application of a Hilbert magnitude transformation to the synthetic radargrams to obtain envelopes. Additional smoothing with a 100 ns Gaussian running mean filter adjusts the visual effect of the shorter FD-source signal to that of the broader RES reflection characteristics.

To reduce the effect of differences in resolution and statistical uncertainty of the various ice-core measuring devices on the synthetic results discussed below, we first apply a 2 cm running mean to all input data. This filter length is below the typical peak width of conductivity signals (e.g. from volcanic eruptions). Statistical noise is thus reduced, but the signal is preserved. The characteristics of  $\epsilon'$  show fluctuations at scales of centimeters to decimeters. As will be shown next, these are related to the measurements so that additional filtering is necessary to recover the reflections present in the RES reference radargrams.

### 3.3. RES vs FD: the role of $\epsilon'$

Over the whole travel-time range of 2–26  $\mu\text{s}$  the comparison of the synthetic radargram  $S_1$  calculated from DEP data, with an additional 0.2 m running mean filter applied to  $\epsilon'$  (Table 1), shows few features in common with the RES reference radargrams  $R_{1,2}$  (Fig. 3). However, the synthetic radargram  $S_3$ , based on  $\epsilon'$  data filtered with a 20 m window and  $\epsilon''$  data with a 0.02 m running mean, contains several events which are found in both reference radargrams. The higher variability in  $S_1$  reflectivity relative to that of radargram  $S_3$  implies that the density signal underlying  $S_1$

is too noisy to reproduce reflections present in RES radargrams. Moreover, the stronger decrease of reflected magnitude in  $S_1$  with travel time beyond 10  $\mu\text{s}$  in comparison to  $S_3$  indicates that the unrealistic noise present in  $\epsilon'$  produces higher reflection loss, meaning that less energy is transmitted to deeper ice.

A second set of numerical modeling runs based on the GAP-density and DEP-conductivity records in the depth range 0–450 m (a time range of 5  $\mu\text{s}$ ) produces the same result ( $S_2$  and  $S_4$  in Fig. 3). Despite the different origin of the GAP-density data, low-pass filtering on the order of tens of meters of  $\epsilon'$  ( $S_4$ ) is necessary to achieve an agreement in the reflection pattern, with the synthetic radargram  $S_3$ , as well as the reference radargrams  $R_1$  and  $R_2$ . Therefore density signals derived from either DEP or GAP contain too much noise to reproduce radargrams with a sufficiently high SNR for regions below the firn–ice transition, in a depth range where conductivity signals become important. In the remaining part of the paper we consequently restrict our RES–FD comparison to synthetic data for which  $\epsilon'$  has been filtered over 20 m. Note that the smoothing has a negligible influence on the travel-time–depth relation (which depends on integrated  $\epsilon'$ ); it merely improves the quality of reproduced reflections.

### 3.4. RES vs FD: characteristic peaks and time shift

A number of reflection patterns visible in the RES reference radargrams  $R_1$  and  $R_2$  are reproduced in the synthetic radargram  $S_3$  (Fig. 3). However, the synthetic reflections in  $S_3$ , which is based on  $\epsilon'_{\text{ice}} = 3.094$ , occur earlier than the corresponding RES signals. To reduce this systematic time shift we model another set of synthetic radargrams  $S'_i$ ,  $i = 3, 5$  (Fig. 3), based on  $\epsilon^*$  calculated with  $\epsilon'_{\text{ice}} = 3.20$  in the forward mixing application at 150 MHz of the DECOMP formula (2). Possible reasons for this observation will be discussed below.

A cross-correlation analysis of the synthetic radargrams with the reference radargrams (denoted by  $S \times R$ ) for the time interval 10–26  $\mu\text{s}$  demonstrates the improved agreement (Fig. 4). (As density variations contribute to reflections down to 10  $\mu\text{s}$ , extending the cross-correlation to shorter travel times includes the uncertainty related to density measurements and leads to less clear results, but is nevertheless feasible.) Prior to cross-correlation all synthetic and RES radargrams are unified to a common sample interval of 1 ns by linear interpolation. The cross-correlation is applied to the logarithmic magnitudes, which are, in the case of the synthetic radargrams, linearly scaled with time to compensate for the RES system's pre-amplification, and for the progressive decrease of magnitudes caused by geometric spreading and losses. The cross-correlation function of  $S_3 \times R_1$  and  $S_3 \times R_2$  has a broad maximum (Fig. 4).  $S_3$  leads  $R_1$  and  $R_2$  by 164 and 153 ns, with correlation maxima of 0.69 and 0.65, respectively. The cross-correlation of  $S'_3 \times R_1$  and  $S'_3 \times R_2$  results in slightly changed maximum correlation coefficients of 0.64 and 0.66, respectively. However, the time shift now changes to a lag of  $S'_3$  with respect to  $R_1$  and  $R_2$  of 36 and 12 ns, respectively, that is only 1–3 RES sample points. Moreover, the cross-correlation function related to  $S'_3$  shows a more pronounced peak of maximum correlation than is the case for  $S_3$ . Based on these results, the in situ travel time underlying the RES radargrams appears to be about 1.6% lower than that arising from the ice-core data in

the synthetic radargrams. To identify the originating depth of reflections, our main goal, we use ice-core data processed with  $\varepsilon'_{ice} = 3.20$  for our further modeling. The related synthetic traces are marked with primed symbols ( $S'_i$ , where only  $i = 3$  and  $5$  will be used; see Table 1).

Several sections of  $S'_3$  show exceptionally good agreement with  $R_1$  and  $R_2$  (Fig. 5). Most prominent are the series of signals at 5–6  $\mu\text{s}$  and 19.5–20.5  $\mu\text{s}$ , the double peaks at 12.6 and 13.7  $\mu\text{s}$ , and the single events at 7.2, 7.7, 10.2, 15.5, 18.4, 22.1 and 24.7  $\mu\text{s}$ . Not only do the times of the reflections correspond to each other, in several cases their structures are also similar. For example, the narrow double peak at 12.6  $\mu\text{s}$ , almost at the limit of temporal resolution in the RES radargrams, is reproduced in the synthetic radargram. Distressingly, the synthetic reflection at 21.1  $\mu\text{s}$  occurring in  $S'_3$  has no counterpart in  $R_1$  or  $R_2$ . Possible reasons are discussed at the end of section 4.3.

To investigate the reproducibility of the above comparison based on DEP conductivity, we calculate another synthetic radargram, based on ECM conductivity ( $S'_5$ ; Table 1). The reflection sequences (Figs 3 and 5) are in general very similar to  $S'_3$ , especially at 5–6, 7.7, 10–12, 12.6, 13.8, 15.5, 18.4, 19.5 and 22.1  $\mu\text{s}$ . However, the reflections resulting from ECM conductivity are less significantly greater than the background variability, compared to the reflections from DEP conductivity (e.g. at 12.6 and 15.5  $\mu\text{s}$ ). The low amplitudes of  $S'_5$  around 7.3  $\mu\text{s}$  are caused by missing ECM data. The reflections produced by DEP conductivity at 19.8–20.5 and 24.7  $\mu\text{s}$  are not reproduced by the ECM conductivity.

## 4. RESULTS AND DISCUSSION

### 4.1. Depth and type of reflector origin

Having identified a number of reflections in the reference radargrams that are reproduced in the synthetic radargrams, we now proceed to determine the physical origin of the synthetic peaks, and thus their originating depth. A correlation between conductivity and reflections has been demonstrated by other studies (Hempel and others, 2000; Miners and others, 2002). We therefore test if individual conductivity peaks present in the DEP and ECM data are also responsible for the strong reflections. (Remember that the permittivity for all  $S_3$  radargrams is smoothed so that all synthetic reflections should be caused only by conductivity signals.) A number of strong conductivity peaks in the  $\varepsilon^*$  profile are removed (Table 2). The gaps are then closed by linear interpolation (Fig. 6). All of the considered conductivity peaks rise about 2–5 times above the background conductivity of  $\sim 10 \mu\text{S m}^{-1}$ , are less than 0.5 m wide and are most likely of volcanic origin. The synthetic radargrams calculated from these data with truncated conductivity peaks (denoted with a tilde,  $\tilde{S}'_3$  and  $\tilde{S}'_5$ ) lack a number of the prominent reflections present in  $S'_3$  and  $S'_5$ , respectively, which have counterparts in the RES radargrams (Fig. 5). For  $\tilde{S}'_3$ , clear correspondence occurs for the reflections at 7.2, 7.7, 12.6, 13.7, 15.5, 18.4, 22.1 and 24.7  $\mu\text{s}$ . In these unambiguous cases the good agreement between synthetic and reference radargrams and the identification of reflection origins enables us to relate the travel time observed in the RES radargrams to the depth of the removed single conductivity peaks. For  $\tilde{S}'_5$ , the agreement and effect of the truncation is somewhat different. Unambiguous cases occur

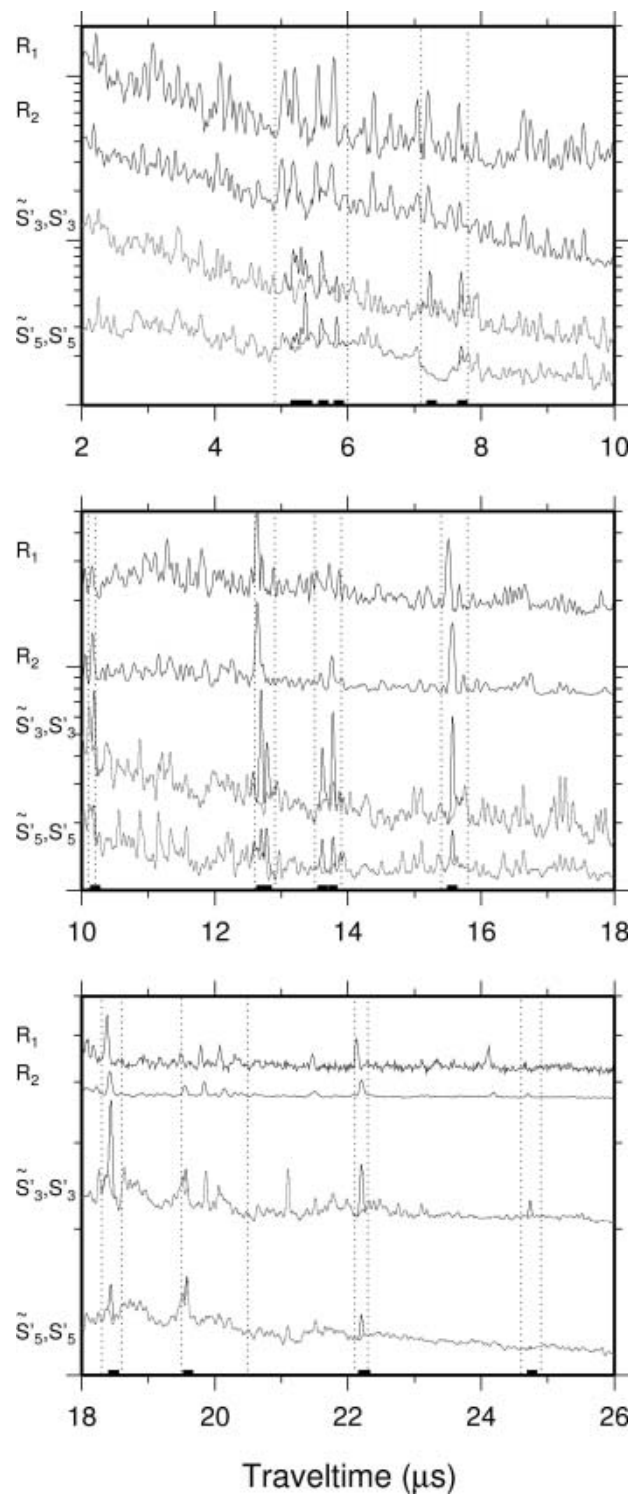


**Fig. 5.** Comparison of RES- and FD-radargram envelopes on a logarithmic scale in arbitrary units. For nomenclature of FD radargrams see Table 1. On top of  $S'_3$  (black) radargram  $\tilde{S}'_3$  (gray) is plotted. Reflections not present in  $\tilde{S}'_3$  therefore appear black. The same is the case for  $S'_5$  and  $\tilde{S}'_5$ . Dominant reflections mentioned in the text are enframed by gray dotted lines. Black boxes on the x axis indicate truncated conductivity peaks used in  $\tilde{S}'_3$  and  $\tilde{S}'_5$ . No time-variant scaling is applied above 18  $\mu\text{s}$ . Beyond 18  $\mu\text{s}$  the square root of  $S'_i$  magnitudes multiplied by travel time is displayed to compensate for logarithmic pre-amplification and decreasing SNR of the reference radargrams.

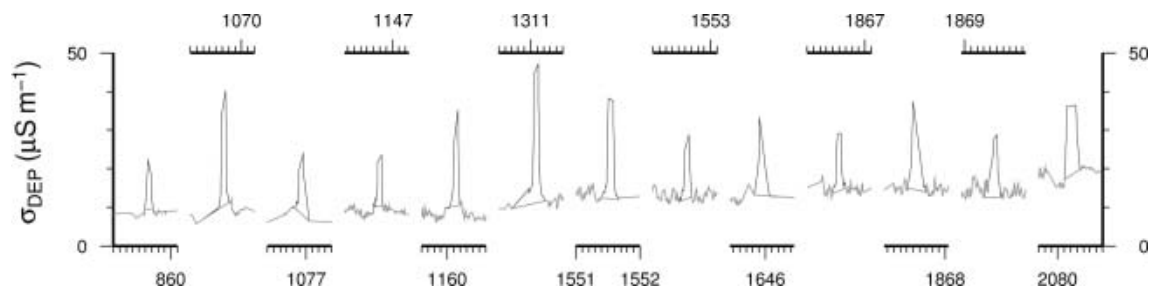


**Fig. 6.** DEP-conductivity peaks (black) for the depth range 800–2100 m ( $\sim 10$ – $25 \mu\text{s}$ ), considered in the sensitivity study to calculate  $S'_3$  for comparison with  $S_3$ . The peaks are removed and the gaps subsequently linearly interpolated (gray), plotted on top of the original curve. Each x-axis segment covers 1 m depth with ticks every 0.1 m.

at 12.6 and 19.5  $\mu\text{s}$ . The RES travel times are taken from  $R_1$ , as this radargram stems from a continuous long-distance profile which is closest to EDML, in contrast to the spatially confined radargram  $R_2$ . We determine the travel time at maximum amplitudes for ten reflections (Table 2). They are accurate with respect to other reflections to within one sample interval, in our case 13 ns.

Two observations indicate not only that single large conductivity peaks cause reflections, but that constructive interference between reflected signals also occurs. The reflections at 18.4 and 22.1  $\mu\text{s}$  require that a series of two and three conductivity peaks, respectively, has to be truncated to completely remove the reflections (Table 2). Interpolation of only one peak of the series merely results in a reduced amplitude of the corresponding reflection. In other cases, the truncation of conductivity peaks does not lead to a significant change in the reflection structure. For instance, the reflection sequence in the range 5–6  $\mu\text{s}$ , the three broad reflections from 19.5 to 20.5  $\mu\text{s}$  and the single reflection at 10.2  $\mu\text{s}$ .

#### 4.2. Error analysis

The accuracy of the established travel-time–depth relations differs for the different types of reflections selected here. According to Ricker's criterion for resolution limits, two signals can be resolved if the separation of their maxima is larger than the full width at half maximum. The RES reflections typically have a full width at half maximum of some 50 ns travel time, which corresponds to about 4 m depth in solid ice. For the processed synthetic traces this value is around 25 ns or 2 m, the higher accuracy because of the shorter source wavelet. Where a single strong conductivity peak causes a synthetic reflection which is in accordance with the RES radargrams, the relation of reflection travel time and reflector depth is unambiguous. The centers of the conductivity peaks in the DEP profile are taken as the depths of origin of the reflections, and the peak width determines the accuracy in depth (Table 2). As all conductivity peaks are less than 0.5 m wide, the error of the depth estimate is less than  $\pm 0.5$  m. This accuracy cannot be achieved for reflections stemming from constructive interference occurring at closely spaced conductivity peaks, such that the resolution criterion given above is not fulfilled. Nevertheless, it is still possible to pin down the depth of origin, though with a larger uncertainty. The two conductivity peaks related to the reflection at 18.4  $\mu\text{s}$  are separated by 1.1 m and together cover a total depth range of 1.3 m, implying a depth estimate accurate to within  $\pm 0.7$  m. The

series of three peaks from 1866.5 to 1869.6 m are separated by at most 1.9 m and cover a range of 3.1 m, which is still smaller than the possible resolution of the RES radargrams. In other cases, for instance for the groups of reflections around 5.3 and 19.5–20.5  $\mu\text{s}$ , several meters of the conductivity profile have to be truncated to completely remove the reflection signature. The uncertainty of the depth estimates in these cases ranges from 2 to 5 m, depending on the profile structure.

##### 4.2.1. Inferences on physical properties

The mean wave speeds are calculated from the surface to the reflector depths, and show a small minimum at intermediate depth (Table 2). In addition to travel-time uncertainties, the logged ice-core depth is subject to errors which enter the wave-speed estimates. They mainly arise from hole inclination, core relaxation, temperature dependence of measuring devices and lost core fraction. Although the individual errors are small, logging-depth errors could add up to meters over an ice core of several kilometers. The wave speeds have an accuracy of better than  $3 \times 10^5 \text{ m s}^{-1}$  in the case of a single conductivity peak as reflection origin. The uncertainty increases to up to  $7 \times 10^5 \text{ m s}^{-1}$  if the depth of origin is less clear, either due to ambiguities in the reflection pattern or large errors in logging depth. A thorough discussion of the wave-speed–depth profile and errors requires comparison with logged temperature and crystal orientation fabric data, which is beyond the scope of this paper.

Our results rely on the correlation between reflections in RES and synthetic radargrams. Apart from manual inspection, the cross-correlation analysis shows that correction of  $\epsilon'_{\text{ice}}$  from 3.094 to 3.20 leads to improved agreement between the reflection patterns. An exact match of RES and synthetic radargrams was possible for a slightly different value of  $\epsilon'_{\text{ice}}$ , along with a zero time-lag of the cross-correlation function, but it does not change our results and is not necessary for the purpose of this study. The most comprehensive compilation to date of dielectric properties of ice, by Fujita and others (2000), indicates that at 150 MHz only the poorly documented data of W.B. Westphal is available as a laboratory reference. Measurements of artificial and natural single crystal and polycrystalline ice at lower frequencies allow a range of 3.14–3.23 (Fujita and others, 2000). However, indirect deductions from travel times as summarized by Bogorodsky and others (1985, table IX) and Popov and others (2003) indicate that our value of 3.09 is comparable to other estimates. This is supported by the work of Kravchenko and others (2004), who found from



tomography at the South Pole a refractive index of  $1.76 \pm 0.03$  (equal to a permittivity of 3.09) at 150 m depth (although bubbles are still present at this depth). The systematic difference in the  $\varepsilon'_{\text{ice}}$  values from the two methods used here could arise from various technical, physical or methodological factors. For the sake of completeness we briefly discuss possible reasons for the observed variation.

#### 4.2.2. Error in ice-core data

Calculation of the synthetic radargrams fundamentally depends on the ice-core properties. Wilhelms (2005) derived a systematic uncertainty on the order of 1% for  $\varepsilon'_{\text{ice}}$ . Reasons for this uncertainty are the accuracy of the GAP and DEP devices as well as inversion of the DECOMP formula. The application of forward mixing includes the transfer of the dielectric properties from 250 kHz to 150 MHz. Frequency dependence and the slightly anisotropic behavior of ice has been observed and studied by different authors (see Fujita and others, 2000, for a summary). Frequency dependence of dielectric anisotropy is well known, although a gap exists in the MHz range. At 252 K,  $\varepsilon'$  values perpendicular (parallel) to the *c* axis are 3.18 (3.21) at 1 MHz and 3.13 (3.16) at 9.7 GHz (Fujita and others, 2000). For a temperature increase of 40 K both components increase on the order of 1% for the temperature ranges observed in ice sheets (Fujita and others, 2000). The applied frequency scaling could, in principle, also contribute to the observed difference in  $\varepsilon'_{\text{ice}}$  of the methods applied here, although the relaxation frequency of ice is below 10 kHz (Bittelli and others, 2004) and should have a negligible influence in the MHz range. In any case, neglecting relaxation would have the opposite effect, namely lead to an overestimated permittivity.

#### 4.2.3. System errors

The reference radargrams depend on the RES system properties. The statistical variation of the length of a sample interval of the RES system is reduced to below 0.5% by the system's 200-fold averaging procedure for each stored trace. However, we cannot exclude a small dependence on operation temperature and ambient pressure. Prior to and after ice-sheet campaigns, the RES system's calibration is checked with mirror flights over sea ice and open water by comparing RES and radar-altimetry altitudes. Differences are around 0.5%.

#### 4.2.4. Geometrical errors

Logging depths are subject to small uncertainties, as mentioned above, and the internal structure is not parallel to the surface, but has small gradients of 0–0.04. The separation of  $R_1$  and EDML by  $\sim 100$  m results in small differences between the reflector depths determined from the EDML profiles and the real depths of origin of the matched reflections at the site of  $R_1$ . The same is, of course, true for  $R_2$ . To completely explain the observed difference by sloping internal layers, however, would require the depth at the location of  $R_1$  to be more than 1% higher. This corresponds to a slope  $>0.2$ , which is not observed.

Unfortunately, we cannot provide a final physical interpretation because of the various systematic and partly unknown measurement uncertainties involved. We have to assume that several of the above factors contribute to the difference.

**Table 2.** Travel-time–depth relationship for selected reflections from trace  $R_1$

Travel time	Width	Depth range	Peak width	Mean wave speed
ns	ns	m	m	$\times 10^8 \text{ m s}^{-1}$
Single peak				
7201	75	611.0–611.4	0.4	1.698
7665	55	650.1–650.4	0.3	1.697
12 628	55	1069.6–1069.8	0.2	1.694
12 709	45	1076.8–1077.0	0.2	1.695
13 527	45	1146.6–1146.9	0.3	1.696
13 716	50	1160.0–1160.2	0.2	1.692
15 502	75	1310.8–1311.2	0.4	1.691
24 666	20	2080.0–2080.4	0.4	1.687
Double peak				
18 385	50	1551.4–1551.6	0.2	1.688
		1552.5–1552.7	0.2	1.689
Triple peak				
22 128	50	1866.5–1866.7	0.2	1.687
		1867.4–1867.7	0.3	1.688
		1869.3–1869.6	0.3	1.690

Notes: Travel times are taken from  $R_1$ , ranges from the truncated conductivity peaks from the DEP-conductivity profile (Fig. 6). Mean wave speed is calculated for the travel time from the surface to the reflector depth.

### 4.3. Comparison to other methods

Usually a certain wave-speed–depth function is integrated from the surface to a certain depth to determine the relevant travel time. As any wave-speed estimate is subject to an error, the integration results in an increasing absolute uncertainty with increasing travel time and depth and thus also for the subsequent travel-time–depth conversion. A relative error in wave speed is linearly translated into an equivalent error in depth.

The method introduced here significantly reduces this relative uncertainty by correlating synthetic and RES radargrams in the time domain based on reflection patterns to identify the reflection origin in the depth domain of the ice-core data. Given the physical properties, the model produces the reflections at the right position and enables us to accurately connect reflectors and ice-core properties. Our travel-time–depth relationship is subject to an absolute uncertainty, which mainly depends on the quality of correspondence between the RES and synthetic reflections. Simultaneously, it takes into account the small depth-dependent variations of wave speed. Given a 1% uncertainty in measured wave speeds (a realistic estimate as demonstrated in Fig. 1), the corresponding depth uncertainty for an ordinary travel-time–depth conversion will likewise be 1%, increasing from 1 m at 100 m depth to 20 m at 2000 m depth. In contrast, our travel-time–depth relationship established above is only subject to an absolute error on the order of 1 m, independent of depth. This simple example illustrates that our method is therefore especially useful for deeper reflections.

A tough constraint for reliable functionality is put on the method by the high SNR demanded of RES and synthetic radargrams. As demonstrated, RES data with high SNR can be produced by increased spatial and temporal coverage. Whereas this is no problem for ground-based surveys, it might not be always possible during airborne measurements.

In polar ice, reflection coefficients for electromagnetic waves at radio frequencies are dominated by changes in  $\epsilon'$ , and are less sensitive to impedance contrasts of  $\epsilon''$ . Masking of most reflections originating from conductivity peaks in the synthetic radargrams by noise in the density profiles can be overcome by low-pass filtering of  $\epsilon'$ . Unfortunately, this also eliminates the information related to small-scale variations in  $\epsilon'$  (from permittivity or anisotropy) in the synthetic radargram. This explains why the agreement of RES and synthetic traces is better below 10  $\mu\text{s}$  than above.

In general, core breaks or only a few centimeters of cracks could also easily mask reflections from conductivity peaks or lead to a rejection of a core section in the quality check. Apart from the difference in conduction mechanisms, this is probably one reason why some reflectors appear in the DEP radargrams, but not in the ECM radargrams (e.g. at 19.8–20.5 and 24.7  $\mu\text{s}$  Fig. 5). In addition, it can also happen that reflections in the reference radargrams are not reproduced by the DEP or the ECM conductivity. As recently shown by Wolff and others (2005), it is difficult to reproduce the conductivity profile for replicate ice cores. In their study at Dome Concordia, two 800 m long conductivity profiles of two ice cores 10 m apart do reproduce individual peaks, but their magnitude varies, typically by a factor of 1.5. Some signals are even completely missing in one of the cores. It is therefore unlikely that synthetic radargrams will reproduce all the RES radargram peaks, even if the measurements take place at exactly the same location, and more so if the locations are separated by a few tens to hundreds of meters.

## 5. CONCLUSIONS

We have presented a method to determine the depth of origin of reflections observed in RES profiles that is more accurate than previous, standard methods. We find that single conductivity peaks are responsible for the majority of individual reflections, especially in the intermediate and deeper parts of the ice sheet, complementing earlier findings on reflection origin (Millar, 1982; Siegert and others, 1998; Miners and others, 2002). Together with the observed insensitivity of the numerical model results to the type of electrical conductivity data used as an input, this implies that the approach can be applied at most deep-drilling locations, as RES and conductivity profiling are standard measurements and are usually available. Moreover, coarse-resolution density profiles, and possibly even theoretical assumptions for the density distribution with depth, are sufficient as the applied physical properties for the pure-ice fraction can be calibrated within a reasonable uncertainty limit by cross-correlation analysis. Apart from reflection origin we also demonstrate the application to determine the in situ permittivity of the pure-ice fraction and the wave speed–depth function.

The most significant potential, however, lies in the connection of RES and ice-core profiles for the synchronization of deep ice cores. A number of authors proved the long-range traceability of internal reflections in Antarctica (e.g. Siegert and Hodgkins, 2000; Steinhage and others, 2001; Jacobel and Welch, 2005) to connect drilling locations. As demonstrated here, we are now able to identify the origin of selected individual reflections to within 1 m accuracy in depth, even for a lower RES resolution, given that single events cause the reflections. Performing a comparable study at either end of RES profiles that connect deep-drilling

locations imposes sound geophysical constraints on the age–depth scales of the ice cores. These constraints are independent of other dating methods, which are usually based on ice-sheet modeling or ice-core records like gas and isotope profiles. Another application is the accurate dating of ice cores drilled in outcropping older ice (Siegert and others, 2003), where no continuous temporal record is available. The good coverage of Greenland with RES profiles combined with this method should be used to improve the accuracy of age–depth distributions. In Antarctica, we hope that the connection of all deep-drilling locations by high-resolution RES, for instance during the IPY 2007/08, will provide a fundamental basis for a comprehensive age–depth map to improve understanding of ice-sheet evolution and phase relations of climate change.

## ACKNOWLEDGEMENTS

During the review process we had some stimulating discussions with J. Moore and another, anonymous, reviewer. We greatly acknowledge and appreciate the effort they put into their reviews and suggestions. Preparation of this work was supported by the Deutsche Forschungsgemeinschaft grant WI 1974/2 and an 'Emmy Noether' scholarship EI 672/1 to O.E. This work is a contribution to the European Project for Ice Coring in Antarctica (EPICA), a joint ESF (European Science Foundation)/EC scientific program, funded by the European Commission and by national contributions from Belgium, Denmark, France, Germany, Italy, the Netherlands, Norway, Sweden, Switzerland and the United Kingdom. This is EPICA publication No. 155.

## REFERENCES

- Annan, A.P. and J.L. Davis. 1976. Impulse radar sounding in permafrost. *Radio Science*, **11**(4), 383–394.
- Bittelli, M., M. Flury and K. Roth. 2004. Use of dielectric spectroscopy to estimate ice content in frozen porous media. *Water Resour. Res.*, **40**(4), W04212. (10.1029/2003WR002343.)
- Bogorodsky, V.V., C.R. Bentley and P.E. Gudmandsen. 1985. *Radioglaciology* Dordrecht, etc., D. Reidel Publishing Co.
- Clarke, G.K.C., N.M. Lhomme and S.J. Marshall. 2005. Tracer transport in the Greenland ice sheet: three-dimensional isotopic stratigraphy. *Quat. Sci. Rev.*, **24**, 155–171.
- Clarke, T.S. and C.R. Bentley. 1994. High-resolution radar on Ice Stream B2, Antarctica: measurements of electromagnetic wave speed in firn and strain history from buried crevasses. *Ann. Glaciol.*, **20**, 153–159.
- Clough, J.W. and C.R. Bentley. 1970. Measurements of electromagnetic wave velocity in the East Antarctic ice sheet. *In Symposium at Hanover 1968 – Antarctic Glaciological Exploration (ISAGE)*. Wallingford, Oxon., International Association of Scientific Hydrology, 115–128. (IAHS Publication 86.)
- Dahl-Jensen, D. and 9 others. 1997. A search in north Greenland for a new ice-core drill site. *J. Glaciol.*, **43**(144), 300–306.
- Dowdeswell, J.A. and S. Evans. 2004. Investigations of the form and flow of ice sheets and glaciers using radio-echo sounding. *Rep. Prog. Phys.*, **67**, 1821–1861.
- Eisen, O., U. Nixdorf, F. Wilhelms and H. Miller. 2002. Electromagnetic wave speed in polar ice: validation of the common-midpoint technique with high-resolution dielectric-profiling and  $\gamma$ -density measurements. *Ann. Glaciol.*, **34**, 150–156.
- Eisen, O., F. Wilhelms, U. Nixdorf and H. Miller. 2003. Revealing the nature of radar reflections in ice: DEP-based FDTD forward modeling. *Geophys. Res. Lett.*, **30**(5), 1218–1221.

- Eisen, O., W. Rack, U. Nixdorf and F. Wilhelms. 2005. Characteristics of accumulation around the EPICA deep-drilling site in Dronning Maud Land, Antarctica. *Ann. Glaciol.*, **41**, 41–56.
- Evans, S. 1965. Dielectric properties of ice and snow – a review. *J. Glaciol.*, **5**(42), 773–792.
- Fahnestock, M.A., W. Abdalati, S. Luo and S. Gogineni. 2001. Internal layer tracing and age–depth–accumulation relationships for the northern Greenland ice sheet. *J. Geophys. Res.*, **106**(D24), 33,789–33,797.
- Fisher, E., G.A. McMechan and A.P. Annan. 1992. Acquisition and processing of wide-aperture ground-penetrating radar data. *Geophysics*, **57**(3), 495–504.
- Fortin, R. and R. Fortier. 2001. Tomographic imaging of a snowpack. In *Proceedings of the 58th Annual Eastern Snow Conference*. Hanover, NH, US Army Engineer Research and Development Center–US Army Cold Regions Research and Engineering Laboratory.
- Frezzotti, M., S. Gandolfi and S. Urbini. 2002. Snow megadunes in Antarctica: sedimentary structure and genesis. *J. Geophys. Res.*, **107**(D18), 4344. (10.1029/2001JD000673.)
- Fujita, S., T. Matsuoka, T. Ishida, K. Matsuoka and S. Mae. 2000. A summary of the complex dielectric permittivity of ice in the megahertz range and its applications for radar sounding of polar ice sheets. In Hondoh, T., ed. *Physics of ice core records*. Sapporo, Hokkaido University Press, 185–212.
- Hammer, C.U. 1980. Acidity of polar ice cores in relation to absolute dating, past volcanism, and radio-echoes. *J. Glaciol.*, **25**(93), 359–372.
- Hargreaves, N.D. 1978. The radio-frequency birefringence of polar ice. *J. Glaciol.*, **21**(85), 301–313.
- Hempel, L., F. Thyssen, N. Gundestrup, H.B. Clausen and H. Miller. 2000. A comparison of radio-echo sounding data and electrical conductivity of the GRIP ice core. *J. Glaciol.*, **46**(154), 369–374.
- Jacobel, R.W. and S.M. Hodge. 1995. Radar internal layers from the Greenland summit. *Geophys. Res. Lett.*, **22**(5), 587–590.
- Jacobel, R.W. and B.C. Welch. 2005. A time marker at 17.5 kyr BP detected throughout West Antarctica. *Ann. Glaciol.*, **41**, 47–51.
- Jacobel, R.W., A.M. Gades, D.L. Gottschling, S.M. Hodge and D.L. Wright. 1993. Interpretation of radar-detected internal layer folding in West Antarctic ice streams. *J. Glaciol.*, **39**(133), 528–537.
- Jezek, K.C. and E.A. Roeloffs. 1983. Measurements of radar wave speeds in polar glaciers using a down-hole radar target technique. *Cold Reg. Sci. Technol.*, **8**(2), 199–208.
- Kanagaratnam, P., S.P. Gogineni, N. Gundestrup and L. Larsen. 2001. High-resolution radar mapping of internal layers at the North Greenland Ice Core Project. *J. Geophys. Res.*, **106**(D24), 33,799–33,811.
- Karlöf, L. 2004. Temporal and spatial variability of snow accumulation and redistribution, and its impact on the interpretation of ice cores. (PhD thesis, University of Oslo.)
- Karlöf, L. and 11 others. 2005. Accumulation variability over a small area in east Dronning Maud Land, Antarctica, as determined from shallow firn cores and snow pits: some implications for ice-core records. *J. Glaciol.*, **51**(174), 343–352.
- Kohler, J., J.C. Moore and E. Isaksson. 2003. Comparison of modelled and observed responses of a glacier snowpack to ground-penetrating radar. *Ann. Glaciol.*, **37**, 293–297.
- Kovacs, A., A.J. Gow and R.M. Morey. 1995. The in situ dielectric constant of polar firn revisited. *Cold Reg. Sci. Technol.*, **23**(3), 245–256.
- Kravchenko, I., D. Besson and J. Meyers. 2003. In situ measurements of the index of refraction of the south polar firn with RICE detector. *J. Glaciol.*, **50**(171), 522–532.
- Leonard, K., R.E. Bell, M. Studinger and B. Tremblay. 2004. Anomalous accumulation rates in the Vostok ice-core resulting from ice flow over Lake Vostok. *Geophys. Res. Lett.*, **31**(24), L24401. (10.1029/2004GL021102.)
- Looyenga, H. 1965. Dielectric constant of heterogeneous mixtures. *Physica*, **31**(3), 401–406.
- Lythe, M.B., D.G. Vaughan and BEDMAP consortium. 2001. BEDMAP: a new ice thickness and subglacial topographic model of Antarctica. *J. Geophys. Res.*, **106**(B6), 11,335–11,351.
- Maidique, M.A., A. von Hippel, D.B. Knoll and W.B. Westphal. 1971. Transfer of protons through ‘pure’ ice  $I_h$  single crystals. III. Extrinsic versus intrinsic polarization; surface versus volume conduction. *J. Chem. Phys.*, **54**, 150–160.
- Matsuoka, K., S. Uratsuka, S. Fujita and F. Nishio. 2004a. Ice-flow induced scattering zone within the Antarctic ice sheet revealed by high-frequency airborne radar. *J. Glaciol.*, **50**(170), 382–388.
- Matsuoka, K., R. Saito and R. Naruse. 2004b. A novel backpackable ice-penetrating radar system. *J. Glaciol.*, **50**(168), 147–150.
- Millar, D.H.M. 1981. Radio-echo layering in polar ice sheets and past volcanic activity. *Nature*, **292**(5822), 441–443.
- Millar, D.H.M. 1982. Acidity levels in ice sheets from radio echo-sounding. *Ann. Glaciol.*, **3**, 199–203.
- Miners, W.D. 1998. Electromagnetic reflections inside ice sheets. (PhD thesis, Open University.)
- Miners, W.D., A. Hildebrand, S. Gerland, N. Blindow, D. Steinhage and E.W. Wolff. 1997. Forward modeling of the internal layers in radio echo sounding using electrical and density measurements from ice cores. *J. Phys. Chem., Ser. B*, **101**(32), 6201–6204.
- Miners, W.D., E.W. Wolff, J.C. Moore, R. Jacobel and L. Hempel. 2002. Modeling the radio echo reflections inside the ice sheet at Summit, Greenland. *J. Geophys. Res.*, **107**(B8), 2172. (10.1019/2001JB000535.)
- Moore, J.C. 1988. Dielectric variability of a 130m Antarctic ice core: implications for radar sounding. *Ann. Glaciol.*, **11**, 95–99.
- Moore, J.C. and J.G. Paren. 1987. A new technique for dielectric logging of Antarctic ice cores. *J. Phys. (Paris)*, **48** (C1), 155–160.
- Moore, J.C., E.W. Wolff, H.B. Clausen and C.U. Hammer. 1992. The chemical basis for the electrical stratigraphy of ice. *J. Geophys. Res.*, **97**(B2), 1887–1896.
- Moore, J.C., E.W. Wolff, H.B. Clausen, C.U. Hammer, M.R. Legrand and K. Fuhrer. 1994. Electrical response of the Summit–Greenland ice core to ammonium, sulphuric acid, and hydrochloric acid. *Geophys. Res. Lett.*, **21**(7), 565–568.
- Morse, D.L. 1997. Glacier geophysics at Taylor Dome, Antarctica. (PhD thesis, University of Washington.)
- Morse, D.L., E.D. Waddington and E.J. Steig. 1998. Ice age storm trajectories inferred from radar stratigraphy at Taylor Dome, Antarctica. *Geophys. Res. Lett.*, **25**(17), 3383–3386.
- Murray, T. and 6 others. 2000. Glacier surge propagation by thermal evolution at the bed. *J. Geophys. Res.*, **105**(B6), 13,491–13,507.
- Neftel, A., E. Moor, H. Oeschger and B. Stauffer. 1985. Evidence from polar ice cores for the increase in atmospheric CO<sub>2</sub> in the past two centuries. *Nature*, **315**, 45–47.
- Nereson, N.A., C.F. Raymond, R.W. Jacobel and E.D. Waddington. 2000. The accumulation pattern across Siple Dome, West Antarctica, inferred from radar-detected internal layers. *J. Glaciol.*, **46**(152), 75–87.
- Nixdorf, U. and 6 others. 1999. The newly developed airborne radio-echo sounding system of the AWI as a glaciological tool. *Ann. Glaciol.*, **29**, 231–238.
- Pälli, A. and 6 others. 2002. Spatial and temporal variability of snow accumulation using ground-penetrating radar and ice cores on a Svalbard glacier. *J. Glaciol.*, **48**(162), 417–424.
- Popov, S.V., A.N. Sheremet’ev, V.N. Masolov, V.V. Lukin, A.V. Mironov and V.S. Luchininov. 2003. Velocity of radio-wave propagation in ice at Vostok station, Antarctica. *J. Glaciol.*, **49**(165), 179–183.
- Richardson, C., E. Aarholt, S.E. Hamran, P. Holmlund and E. Isaksson. 1997. Spatial distribution of snow in western Dronning Maud Land, East Antarctica, mapped by a ground-based snow radar. *J. Geophys. Res.*, **102**(B9), 20,343–20,353.
- Richardson-Näslund, C. 2001. Spatial distribution of snow in Antarctica and other glacier studies using ground-penetrating radar. (PhD thesis, Stockholm University.)

- Robin, G.deQ., S. Evans and J.T. Bailey. 1969. Interpretation of radio echo sounding in polar ice sheets. *Philos. T. Roy. Soc. London, Ser. A*, **265**(1166), 437–505.
- Siegert, M.J. 1999. On the origin, nature and uses of Antarctic ice-sheet radio-echo layering. *Prog. Phys. Geog.*, **23**(2), 159–179.
- Siegert, M.J. and R. Hodgkins. 2000. A stratigraphic link across 1100 km of the Antarctic ice sheet between the Vostok ice-core site and Titan Dome (near South Pole). *Geophys. Res. Lett.*, **27**(14), 2133–2136.
- Siegert, M.J., R. Hodgkins and J.A. Dowdeswell. 1998. A chronology for the Dome C deep ice-core site through radio-echo layer correlation with the Vostok ice core, Antarctica. *Geophys. Res. Lett.*, **25**(7), 1019–1022.
- Siegert, M.J., R.C.A. Hindmarsh and G.S. Hamilton. 2003. Evidence for a large surface ablation zone in central East Antarctica during the last Ice Age. *Quat. Res.*, **59**, 114–121.
- Siegert, M.J. and 9 others. 2004. Ice flow direction change in Interior West Antarctica. *Science*, **305**(5692), 1948–1951.
- Spikes, V.B., G.S. Hamilton, S.A. Arcone, S. Kaspari and P. Mayewski. 2004. Variability in accumulation rates from GPR profiling on the West Antarctic plateau. *Ann. Glaciol.*, **39**, 238–244.
- Steinhage, D., U. Nixdorf, U. Meyer and H. Miller. 2001. Subglacial topography and internal structure of central and western Dronning Maud Land, Antarctica, determined from airborne radio echo sounding. *J. Appl. Geophys.*, **47**, 183–189.
- Steinhage, D., O. Eisen and H.B. Clausen. 2005. Regional and temporal variation of accumulation around NorthGRIP derived from ground-penetrating radar. *Ann. Glaciol.*, **42**, 326–330.
- Vaughan, D.G., P.S. Anderson, J.C. King, G.W. Mann, S.D. Mobbs and R.S. Ladkin. 2004. Imaging of firn isochrones across an Antarctic ice rise and implications for patterns of snow accumulation rate. *J. Glaciol.*, **50**(170), 413–418.
- Wilhelms, F. 1996. Leitfähigkeits- und Dichtemessung an Eisbohrkernen. *Ber. Polarforsch.* 191.
- Wilhelms, F. 2000. Messung dielektrischer Eigenschaften polarer Eiskerne. *Ber. Polarforsch.* 367.
- Wilhelms, F. 2005. Explaining the dielectric properties of firn as a density-and-conductivity mixed permittivity (DECOMP). *Geophys. Res. Lett.*, **32**(16), L16501. (10.1029/2005GL022808.)
- Wolff, E., I. Basile, J.R. Petit and J. Schwander. 1999. Comparison of Holocene electrical records from Dome C and Vostok, Antarctica. *Ann. Glaciol.*, **29**, 89–93.
- Wolff, E.W., E. Cook, P.R.F. Barnes and R. Mulvaney. 2005. Signal variability in replicate ice cores. *J. Glaciol.*, **51**(174), 462–468.
- Yee, K.S. 1966. Numerical solution of initial boundary value problems involving Maxwell's equations in isotropic media. *IEEE Trans. Antennas and Propagation*, **14**, 302–307.

MS received 21 September 2005 and accepted in revised form 10 May 2006